NAVAL POSTGRADUATE SCHOOL

MONTEREY, CALIFORNIA

THESIS

STRATIFIED WAKE SIGNATURES GENERATED BY PROPAGATING SUBMERGED BODIES IN THE PRESENCE OF AN ACTIVE INTERNAL WAVE FIELD

by

Jack C. Dougherty

June 2020

Thesis Advisor: Timour Radko
Second Reader: Justin M. Brown

THIS PAGE INTENTIONALLY LEFT BLANK

REPORT DOCUMENTATION PAGE	*Form Approved OMB No. 0704-0188*

1. AGENCY USE ONLY *(Leave blank)*	**2. REPORT DATE** June 2020	**3. REPORT TYPE AND DATES COVERED** Master's thesis

4. TITLE AND SUBTITLE
STRATIFIED WAKE SIGNATURES GENERATED BY PROPAGATING SUBMERGED BODIES IN THE PRESENCE OF AN ACTIVE INTERNAL WAVE FIELD

5. FUNDING NUMBERS
RQNMH

6. AUTHOR(S) Jack C. Dougherty

7. PERFORMING ORGANIZATION NAME(S) AND ADDRESS(ES)
Naval Postgraduate School
Monterey, CA 93943-5000

8. PERFORMING ORGANIZATION REPORT NUMBER

9. SPONSORING / MONITORING AGENCY NAME(S) AND ADDRESS(ES)
Office of Naval Research Washington, DC 20375

10. SPONSORING / MONITORING AGENCY REPORT NUMBER

11. SUPPLEMENTARY NOTES The views expressed in this thesis are those of the author and do not reflect the official policy or position of the Department of Defense or the U.S. Government.

12a. DISTRIBUTION / AVAILABILITY STATEMENT
Approved for public release. Distribution is unlimited.

12b. DISTRIBUTION CODE
A

13. ABSTRACT (maximum 200 words)

This study characterizes the detectability of a stratified wake in the presence of background internal waves using numerical simulations. To achieve this, we conducted numerical simulations on Department of Defense high-performance computing systems using the Massachusetts Institute of Technology general circulation model, which we adapted for wake simulations. The internal waves were generated by forcing fluid motion over the seafloor with the frequency of semi-diurnal tides, while the topography is simulated based on a data-based stochastic model. By varying the magnitude of the forcing, we were able to perform a series of simulations with distinct initial intensities of the internal wave field in the range that reflects typical conditions in the ocean. The submerged body is characterized as an ellipsoid, whose depth and velocity were varied in order to analyze the strength of the signatures in relation to the background noise. Our analysis reveals limited influence of the wave field on the wake's persistence. We also estimate the noise for the turbulent and thermal dissipation rates by taking a time average over a tidal cycle prior to the introduction of the submerged body. Using this noise, we show that, for our parameters, the wake from a submerged body would be undetectable after 30–60 minutes of passage. Finally, we observed that an interaction exists between the wake and the boundary layer that results in turbulence entrainment between both regions of the domain.

14. SUBJECT TERMS modeling, simulation, stratified wakes	**15. NUMBER OF PAGES** 49
	16. PRICE CODE

17. SECURITY CLASSIFICATION OF REPORT	**18. SECURITY CLASSIFICATION OF THIS PAGE**	**19. SECURITY CLASSIFICATION OF ABSTRACT**	**20. LIMITATION OF ABSTRACT**
Unclassified	Unclassified	Unclassified	UU

NSN 7540-01-280-5500

Standard Form 298 (Rev. 2-89)
Prescribed by ANSI Std. 239-18

THIS PAGE INTENTIONALLY LEFT BLANK

Approved for public release. Distribution is unlimited.

STRATIFIED WAKE SIGNATURES GENERATED BY PROPAGATING SUBMERGED BODIES IN THE PRESENCE OF AN ACTIVE INTERNAL WAVE FIELD

Jack C. Dougherty
Lieutenant Commander, United States Navy
BA, Edinboro University of Pennsylvania, 2007

Submitted in partial fulfillment of the
requirements for the degree of

MASTER OF SCIENCE IN METEOROLOGY AND PHYSICAL OCEANOGRAPHY

from the

NAVAL POSTGRADUATE SCHOOL
June 2020

Approved by: Timour Radko
Advisor

Justin M. Brown
Second Reader

Peter C. Chu
Chair, Department of Oceanography

THIS PAGE INTENTIONALLY LEFT BLANK

ABSTRACT

This study characterizes the detectability of a stratified wake in the presence of background internal waves using numerical simulations. To achieve this, we conducted numerical simulations on Department of Defense high-performance computing systems using the Massachusetts Institute of Technology general circulation model, which we adapted for wake simulations. The internal waves were generated by forcing fluid motion over the seafloor with the frequency of semi-diurnal tides, while the topography is simulated based on a data-based stochastic model. By varying the magnitude of the forcing, we were able to perform a series of simulations with distinct initial intensities of the internal wave field in the range that reflects typical conditions in the ocean. The submerged body is characterized as an ellipsoid, whose depth and velocity were varied in order to analyze the strength of the signatures in relation to the background noise. Our analysis reveals limited influence of the wave field on the wake's persistence. We also estimate the noise for the turbulent and thermal dissipation rates by taking a time average over a tidal cycle prior to the introduction of the submerged body. Using this noise, we show that, for our parameters, the wake from a submerged body would be undetectable after 30–60 minutes of passage. Finally, we observed that an interaction exists between the wake and the boundary layer that results in turbulence entrainment between both regions of the domain.

THIS PAGE INTENTIONALLY LEFT BLANK

Table of Contents

THIS PAGE INTENTIONALLY LEFT BLANK

List of Figures

List of Tables

THIS PAGE INTENTIONALLY LEFT BLANK

List of Acronyms and Abbreviations

Fr	Froude number
MITgcm	Massachusetts Institute of Technology General Circulation Model
NPS	Naval Postgraduate School
Re	Reynold number
Ri	Richardson number
SB	Submerged Body

THIS PAGE INTENTIONALLY LEFT BLANK

Acknowledgments

This thesis would have been impossible were it not for the guidance, contribution and motivation from so many people. First, I would like to thank my thesis advisor, Dr. Timour Radko. His excitement in the classroom made learning a subject that was foreign to me less daunting. His guidance and creativity not only steered me in the right direction but also allowed me to explore and stumble. I would also like to thank Dr. Justin Brown for all of the modifications he made to MITgcm that adapted it for wake simulations as well as for all the time that he committed to mentoring and educating me. This project would have ended at the first command prompt without his guidance and camaraderie. Next, I'd like to acknowledge the work of my predecessors, Zach Moody, Michael Martin, Chris Merriam, Tom Newman, Troy Benbow, and Rino Guerrero for laying the foundation at NPS for stratified wake studies. To my cohort, Jessica Garrett, Jess Rogers, Co Johnson, Wes Davis, Brodie Wells and Kuan-min (Kelly) Kang, thank you all for your friendship, your kindness and your teamwork. You have given me something to aspire to.

Lastly, I would like to thank my family. To my daughters, Annabelle and Fiona, thank you for always being yourselves and making me smile no matter how overwhelmed I was. To my wife, Jenny, I cannot put into words how much I love you and appreciate you as my partner in this adventure. Thank you for all of your love and support. Thank you for all the times you had to pull double duty while I was distracted and putting in long days and late nights. All I can say is thank you, and I love you!

THIS PAGE INTENTIONALLY LEFT BLANK

CHAPTER 1:
Introduction

1.1 Motivation

Since the advent of submarine warfare, militaries across the world have been working to develop methods to detect these underwater assets. Search methodology has largely depended on active and passive sonars to be the work horse for the past hundred years. However, advances such as air-independent propulsion systems and noise-reducing tiles, are being made in order to ensure submarine's reflect and radiate less acoustic energy to inhibit detection. These advances require us to expand our methods of detection. One area of promise lies in the hydrodynamic effects created by a submarine's transit. Submarines and other submerged bodies traversing through a stratified fluid produce a detectable wake by perturbing the background temperature profile and also by the production of small-scale turbulence. This can create a non-acoustic method to detect a submarine's effect on the environment instead of detecting the submarine itself.

1.2 Background

Stratified wakes develop as momentum is transferred from a submerged body to its surrounding environment and can be described by the Reynolds number,

$$\mathrm{Re} = \frac{UL}{\nu}, \tag{1.1}$$

and Froude numbers,

$$\mathrm{Fr} = \frac{U}{NL}, \tag{1.2}$$

where U and L are the submerged body's velocity and diameter, respectively. The fluid's kinematic viscosity is ν and the Brunt-Väisälä frequency, N, determines the oscillation rate

of a vertically displaced fluid parcel,

$$\mathrm{N} = \sqrt{-\frac{\mathrm{g}}{\rho_0}\frac{\partial \rho}{\partial \mathrm{z}}}, \tag{1.3}$$

where g is the acceleration due to gravity, ρ_0 is a reference density, and $\partial\rho/\partial \mathrm{z}$ is the vertical density gradient.

Early experiments by Pao and Kao [1] demonstrated how the wake transitions from laminar to turbulent flow based on the Reynolds number, which is a ratio of inertial to viscous forces. When the Reynolds number is small, the viscosity dominates, and the flow is laminar. As the Reynolds number increases, the wake develops into a von Kármán street. Finally when the Reynolds number is large, the inertial forces dominate the viscous force and the wake becomes turbulent.

As described in Lin and Pao [2], the stratification in the water column inhibits a wake's vertical expansion, which causes the wake to collapse and form flattened vortices. This results in an evolution of the wake over time which can be described by the Froude number, the ratio between inertial and buoyancy forces. At times much less than one buoyancy period, the effects of N are minimal, and the wake evolves in a manner similar to an unstratified one. As the wake collapses, continuity forces it to spread out horizontally, resulting in a flat wake. This creates a meandering in the wake that evolves into horizontal vortices. As proposed by Spedding [3], a universal energy decay rate of these systems shows three distinct phases for the near, intermediate, and late wakes. This evolutionary process occurs over short timescales relative to rotational effects, so the Coriolis force is often neglected. However, Radko and Lorfeld [4] demonstrated that the Coriolis force can influence structures ranging from 10–100 m and should be considered when examining the later stages of the wake (on the order of days to a couple weeks).

A series of laboratory experiments, field studies, and numerical simulations demonstrated that hydrodynamic signatures within the water column could be used for detection. Laboratory experiments by Voropyaev [5] determined under what conditions wakes could penetrate a two-layer fluid and create a detectable signature on the surface. They estimated that near the surface, eddies created by typical self-propelled submerged bodies at a depth of 110

m could be observed. Next, it was shown in the field study conducted by Moody et al [6] that thermal mixing occurs after the submerged body passes and leads to a long-lasting (approximately 2.5 hrs) and detectable change in the thermal stratification. Then, a series of numerical simulations by Radko and Lewis [7] examined the decay rates of stratified wakes in quiescent and turbulent fluids. They showed that the dissipation rates of temperature and momentum, χ and ε, could be used to diagnose the stratified wake's decay. In particular, they found that the simulations with pre-existing convective overturning dissipated the wake most efficiently. By extrapolating their results, they concluded that objects with a 10–meter diameter, moving at 10 ms^{-1} could create a wake that is detectable for four hours after the submerged body's transit.

For this study, we are contrasting the stratified wake produced by a submerged body in two distinct cases: one with an initially quiescent domain and one with an initially turbulent domain. The latter case is depicted in Figure 1.1, where an internal wave field was generated by forcing fluid flow over a bottom topography to create realistic turbulence. The flow was periodic in nature with a frequency matching M2 tides. Once the desired Richardson number, Ri, was achieved, a submerged body was introduced and traversed the domain. We characterize the effects that the submerged body properties, such as speed and depth, have on the wake.

Chapter 2 will address the methodology, including the numerical setup and the governing equations of the simulations. We address our results in Chapter 3, which will cover the morphology, evolution, and decay rates of the wake signals. Finally we discuss our conclusions, the operational relevance of our research, and future research opportunities in Chapter 4.

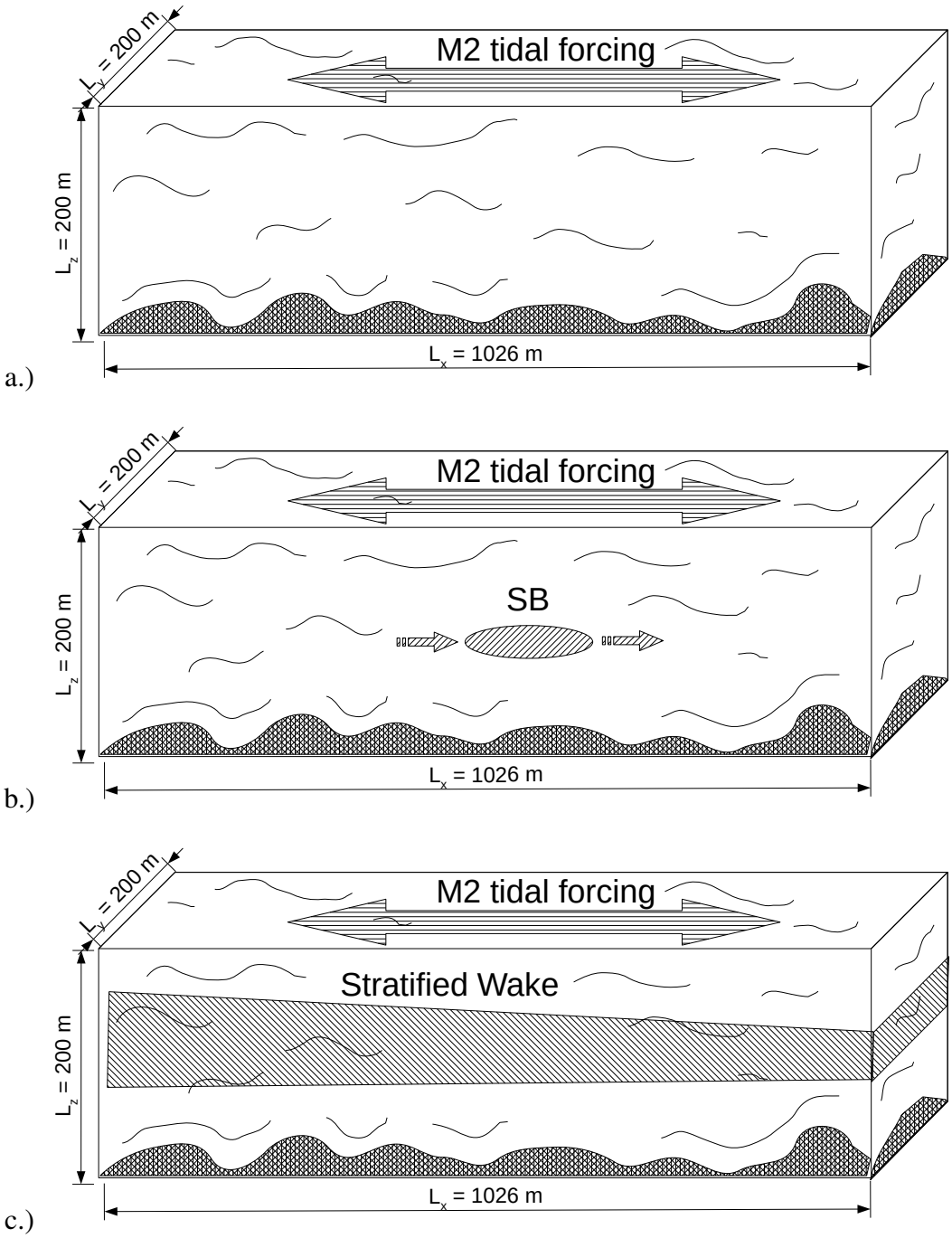

Figure 1.1. Simulation schematic. a.) Fluid flows periodically over topography to generate internal waves. b.) The SB passes through the domain once the internal waves are established. c.) The wake from the SB develops in the internal wave field.

CHAPTER 2:
Methods

2.1 Model Setup

For this study, we use MITgcm (the Massachusetts Institute of Technology General Circulation Model), which is a finite volume code that is designed to handle a wide variety of problems of varying scale, as described in Marshall et al [8]. Our study uses the non-hydrostatic configuration to allow vertical fluid motion within our domain. Under the Boussinesq approximation, the governing equations are described by Equations 2.1 through 2.5:

$$\nabla \cdot \mathbf{u} = 0, \tag{2.1}$$

$$\frac{\rho - \rho_0}{\rho_0} = -\alpha(T - T_0), \tag{2.2}$$

$$\frac{\partial T}{\partial t} + \mathbf{u} \cdot \nabla T = k_T \nabla^2 T + G(T), \tag{2.3}$$

$$\frac{\partial \mathbf{u}}{\partial t} + \mathbf{u} \cdot \nabla \mathbf{u} + f\mathbf{e}_z \times \mathbf{u} = \frac{-1}{\rho_0}\nabla p - \frac{\rho}{\rho_0} g\mathbf{e}_z + \nu \nabla^2 \mathbf{u} + G(u)\mathbf{e}_x, \tag{2.4}$$

$$\frac{\partial \eta}{\partial t} + \nabla_h \cdot (\eta \mathbf{u}) = 0, \tag{2.5}$$

which represent the continuity equation, linear equation of state, temperature equation, momentum equation, and the free surface equation. The vector, $\mathbf{u} = (u, v, w)$, is the total velocity vector, and $\mathbf{e}_x$ and $\mathbf{e}_z$ are unit vectors in the x- and z-directions, respectively. The density is ρ, temperature is T, and p is the pressure. We use a thermal expansion coefficient,

α, of $2 \times 10^{-4} {}^{\circ}\mathrm{C}^{-1}$ and the constant T_0 is a reference value for surface temperature. The Coriolis parameter, f, is approximated as $1 \times 10^{-4} \mathrm{s}^{-1}$, which is appropriate for a typical mid-latitude region as in Radko and Lorfeld [4]. Standard gravitational acceleration, g, is approximated as 9.81 ms^{-2}. The free surface height is η, and the subscript h on ∇_h, implies only the horizontal components of the gradient operator are used. The viscosity, ν, and thermal diffusivity, k_T, are set to $1 \times 10^{-2} \mathrm{m}^2 \mathrm{s}^{-1}$ to approximate the effects of turbulent dissipation. The horizontally uniform source term $G(T)$, in the thermal equation serves as a heat source (sink) to maintain the thermal gradient at the top (bottom) of the domain. In the momentum equation, the source term, $G(u)$, simulates tidal forcing. Both of these source terms will be explained in detail in Section 2.2.

The domain is a rectangular box 1024 m $\times$ 200 m $\times$ 200 m along the x, y, and z axes. Simulations were resolved at the 2–meter scale in all directions. A free surface characterizes the upper boundary to mimic the ocean surface which evolves according to Equation 2.5, and the pressure, p, is set to zero on the surface of $z = \eta$. The lateral boundaries are doubly periodic. The bottom topography is simulated by an anisotropic, stochastic model derived from Sea Beam data, as described by Goff and Jordan [9]. The topography's spectrum, $H(k, l)$ is described by Equation 2.6:

$$H(k,l) \propto \left(1 + \frac{k^2}{k_0^2} + \frac{l^2}{l_0^2}\right)^{-(\beta+1)}, \tag{2.6}$$

where k and l are the wavenumbers in the x and y directions. The roll-off wavenumbers, k_0 and l_0 are both $2\pi \times 1.8 \times 10^{-4} \mathrm{m}^{-1}$, and the high wavenumber slope, β, is -0.55. Through an iterative process we explored the effect that the bottom topography had on the stability of the square of the vertical shear over time. The topographic wavelength range is limited between 90 and 200 m to ensure isotropic terrain in the domain.

It is our goal to seed the domain with internal waves with a characteristic Richardson number. To reach these values, we calculated the mean N^2 over the upper half of the domain using second-order accurate finite differencing. The average value of $(\partial \mathbf{u}/\partial \mathrm{z})^2$ is also calculated over the upper half of the domain by the same method. We define the mean Richardson number as the ratio of these two quantities as in Equation 2.7:

$$\mathrm{Ri}_{avg} = -\frac{g\alpha < \partial T/\partial z >}{< (\partial \mathbf{u}/\partial z)^2 >}, \tag{2.7}$$

where the angled brackets denote the spatial average in the upper half of the domain.

2.2 Forcing Functions

Since the mean Richardson number cannot be calculated a priori, we iterated over forcing amplitude to achieve our desired values of the mean Richardson numbers, based on a 2 m increment, of 5, 10, and 20, which are typical of the ocean, the results of which are shown in Table 3.1. The background oscillating velocity field is given by Equation 2.8,

$$\mathrm{u(t)} = \mathrm{u_0 cos}(2\pi\gamma \mathrm{t}), \tag{2.8}$$

where u_0 is the initial x-velocity, and $\gamma = 2.237\times10^{-5}\mathrm{s}^{-1}$ is the frequency of M2 semidiurnal tides.

We also enforce a mean temperature gradient to prevent the turbulence from homogenizing the thermal gradient. The temperature profile is a linear function of depth as described in Equation 2.9,

$$\overline{T}(z) = T_0 + z\frac{d\overline{T}}{dz}, \tag{2.9}$$

where the quantity $d\overline{T}/dz$, is a constant of $0.014°\mathrm{Cm}^{-1}$ and the reference temperature, T_0, is 1.38°C. This establishes a Brunt-Väisälä frequency, typical of mid-latitudes, with a period of 20 minutes.

The source term, G, from the thermal and momentum equations is defined in terms of a generic variable q is as shown in Equation 2.10:

$$G(q) = \frac{\alpha}{\tau}\overline{q}, \tag{2.10}$$

where τ is a 10 second relaxation constant, $\overline{q}$ is a generic enforced mean field, and α is defined as,

$$\alpha \equiv \frac{-\int_V M\overline{q}(q-\overline{q})\,dV}{\int_V M\overline{q}\cdot\overline{q}\,dV}, \tag{2.11}$$

where the integral is taken over the entire domain, denoted as V. The quantity M is a spatially dependent masking function, which can take values from 0 to 1. For the temperature forcing, the mask is a piecewise function,

$$M = \begin{cases} 1 & 0\text{m} \geq z \geq z_T \\ 0 & z_T \geq z \geq z_B \\ 1 & z_B \geq z \geq -200\text{m}, \end{cases} \tag{2.12}$$

where z_T is the depth at the bottom of the top layer and z_B is the depth at the top of the bottom layer. The masking function begins at the surface where z = 0 m, and goes to the bottom of the domain at z = -200 m. For the momentum forcing, the masking function is unity over the entire domain. The net effect of this forcing term causes the mean field, q, to approach $\overline{q}$.

2.3 Submerged Body

The submerged body is a towed ellipsoid with an 85-meter principal semi-axis in the x direction and a 14-meter diameter in the y- and z-directions. The ellipsoid begins at rest at (0, 0, D), where D is the depth from the surface to the center of the ellipsoid. It then accelerates in the x-direction for 100 m to a maximum velocity, u_{max} $\mathbf{e}_x$; proceeds at that velocity for 650 m; and finally decelerates over another 100 m to rest. After the submerged body returns to rest, the solid boundaries of the object are no longer enforced.

CHAPTER 3:
Results

3.1 Simulations

Once we established turbulence with the desired Richardson numbers, we introduced the submerged body and passed it through the domain at various depths, and velocities as listed in Table 3.1. To identify the observable signals, we examine the dissipation of turbulent kinetic energy, ε, and thermal variance, χ. These quantities highlight small-scale turbulence rather than other transient and intransient features. We define the dissipation rates in Equations 3.1 and 3.2,

$$\chi = 2k_T \left[\left(\frac{\partial T_p}{\partial x} \right)^2 + \left(\frac{\partial T_p}{\partial y} \right)^2 + \left(\frac{\partial T_p}{\partial z} \right)^2 \right] \tag{3.1}$$

$$\varepsilon = \nu \left[\left(\frac{\partial \mathbf{u}}{\partial x} \right)^2 + \left(\frac{\partial \mathbf{u}}{\partial y} \right)^2 + \left(\frac{\partial \mathbf{u}}{\partial z} \right)^2 \right] \tag{3.2}$$

where T_p is the temperature perturbation of the current field with respect to the horizontally averaged temperature field.

We then define $\langle \chi \rangle_\mathrm{t}$ to be the mean of the quantity χ only within the volume where χ exceeds a certain threshold given by $\zeta_\chi \langle \chi \rangle$, where ζ_χ is a constant multiplier and $\langle \chi \rangle$ is the mean of χ throughout the upper half of the domain. This is threshold mean is defined in Equation 3.3,

$$\langle \chi \rangle_t = \frac{\int_V \chi m \, dV}{\int_V m \, dV}, \tag{3.3}$$

where the integrals are taken over the upper 100 meters of the domain. The masking term, m, is a spatially dependent piecewise function that takes on the values of 0 or 1.

Table 3.1. Simulations parameter overview

run	case	Ri_{avg}	depth (m)	velocity (m/s)
1	quiescent	-	-50	5
2	internal waves	5		
3	internal waves	10		
4	internal waves	20		
5	quiescent	-	-25	5
6	internal waves	10		
7	quiescent	-	-50	2.5
8	internal waves	10		
9	quiescent	-	-50	10
10	internal waves	10		

$$m = \begin{cases} 1 & \chi > \zeta_\chi \langle \chi \rangle \\ 0 & \chi < \zeta_\chi \langle \chi \rangle. \end{cases} \tag{3.4}$$

The multiplier, ζ_χ is empirically chosen to be 4.0 to easily differentiate between the direct wake signal and the background turbulence. This ensures that only values greater than $4\langle \chi \rangle$ are included in the calculations. An analogous quantity can be defined for $\langle \varepsilon \rangle_\mathrm{t}$, with a threshold factor given by $\zeta_\varepsilon = 2.0$.

3.2 Conditions Prior to Transit

As described in Section 2.2, we used a forcing function to establish an initially turbulent state prior to introducing the submerged body in our turbulent cases. The parameter u_0 was chosen, to establish a state with the desired mean Richardson numbers in the upper 100 meters of the domain, as outlined in Table 3.2. Over this same region of the domain, we define the characteristic noise as the temporal average of the respective mean threshold value, $\langle \chi \rangle_\mathrm{t}$ or $\langle \varepsilon \rangle_\mathrm{t}$, over one tidal cycle prior to the submerged body's transit. This noise value will serve as a criterion that will determine the viability of detecting a submerged body wake. This value will be compared with wake signatures in the quiescent cases in Section 3.4.

Table 3.2. Conditions prior to transit

Ri_{avg}	u_0 (m/s)	N (rad/s)	$\langle\chi\rangle_\mathrm{t}$ ($^\circ\mathrm{C}^2$ /s)	$\langle\varepsilon\rangle_\mathrm{t}$ (m^2 /s^3)
5	0.42	5.63×10^{-3}	1.31×10^{-5}	1.87×10^{-6}
10	0.40	5.68×10^{-3}	2.51×10^{-6}	6.77×10^{-7}
20	0.38	5.37×10^{-3}	1.71×10^{-6}	3.32×10^{-7}

Figure 3.1 shows the total temperature field and the x-component of the velocity field for the case with a mean Richardson number of 10. The upper half of the domain remains relatively calm, whereas, the lower 100-meter region exhibits an increase in turbulent activity. Below 100 m, the temperature field is well mixed. In the upper 100 m, the x-component of the velocity field is uniform, in accordance with our external forcing, and the mean velocity decreases with depth toward the no-slip boundary at the bottom of the domain, forming a turbulent boundary layer.

3.3 Wake Morphology and Evolution

Figure 3.2, depicts a side-by-side comparison of the thermal dissipation rate, spatially averaged along the direction of travel, $\overline{\chi}$, for the quiescent and turbulent cases from runs 1 and 2. For both cases, the submerged body passed through the domain at a depth of -50 meters with a velocity of 5 ms^{-1}. The turbulent case had a mean Richardson number of 10 prior to the transit. Each plot is a cross-section of the wake averaged along the path of travel and is separated in time by $N\Delta t = 5.14$.

Starting at $Nt = 0$, we observe in both scenarios that the signal remains in the center of the plotted region and is located where the submerged body transited. In the quiescent case, the wake signature is vertically elongated, whereas, the turbulent wake signature is more compact. Below the wake signature in the turbulent case, we see evidence of an increase in $\langle\chi\rangle_\mathrm{t}$ that is not from the submerged body's immediate transit but is instead raising from the lower half of the domain. We can attribute this to entrainment of the nearly isothermal turbulent boundary layer into the upper, stratified region of the simulated domain.

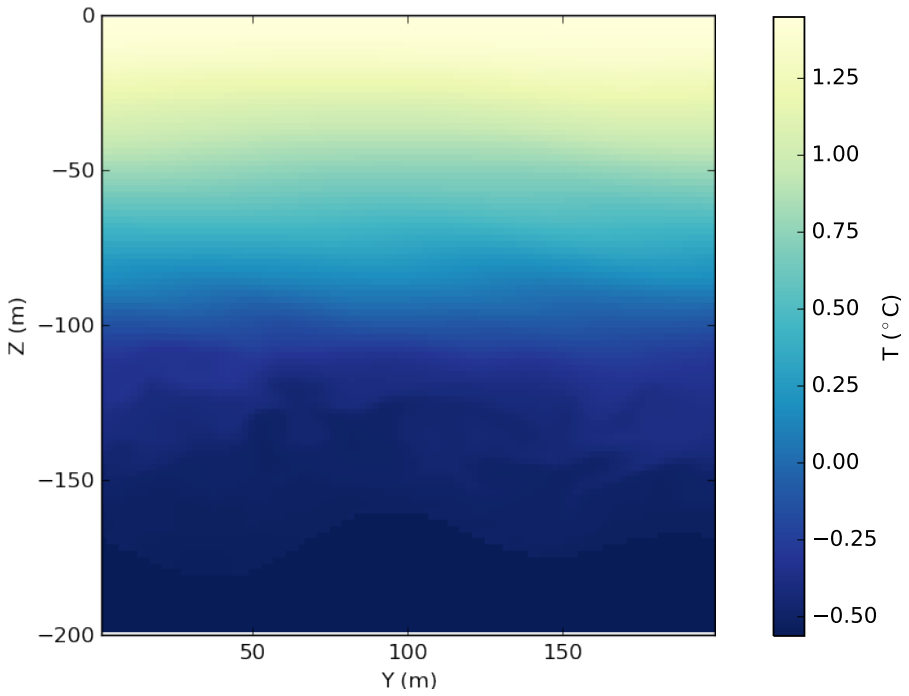

a.)

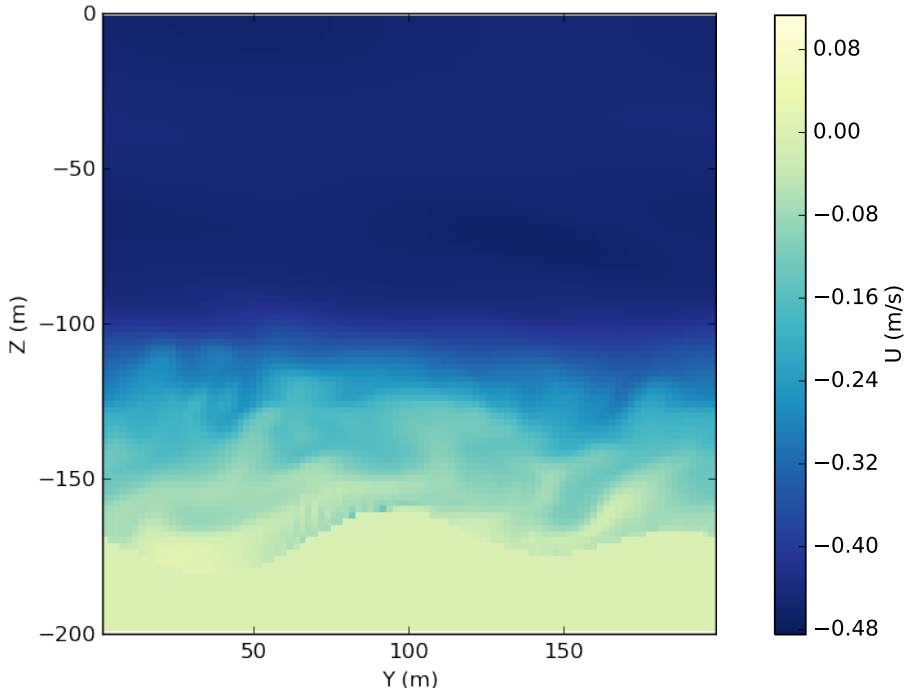

b.)

Figure 3.1. A yz-plane through the entire domain immediately prior to the introduction of the SB. a.) The total temperature field. b.) The x-component of the velocity field.

Fifteen minutes later (Nt = 5.14), the elongated quiescent signal has expanded horizontally and is now more circular. It has also maintained its position in the center of the domain. Conversely, in the turbulent case, the signal is advected by the background flow in the positive y-direction, leading to a 60-meter drift over these 15 minutes. Due to the simulations' periodic boundaries, part of the signal is exiting the right side of the figure and re-entering on the left, but otherwise, this has no substantial effect on our results. The signature billowing up from the bottom half of the domain has risen to a depth of -80 m, with a signal strength comparable to the wake signature and concentrated nearly below the wake. We take this as an indication that the billowing effect may in fact be caused by interactions between the wake and the turbulent boundary layer.

Between a half hour to an hour after the submerged body's transit (Nt = 10.31 to Nt = 20.60), the quiescent signal has substantially collapsed in the vertical direction and has widened in the horizontal direction, which is expected in order to preserve continuity. An hour after the submerged body's passage (Nt = 20.60), the wake has significantly expanded (from 80 m at Nt = 5.14 to 125 m) in the horizontal direction, transitioning from a circular cross-section to an elliptical one. The vertical extent has also significantly decreased as compared with the Nt = 5.14 signal, decreasing from 60 m, to 40 m. During this same time period, the corresponding turbulent case continues to drift to the right and is becoming more diffuse as the previously circular cross-section disperses. Forty-five minutes after the submerged body transited, the turbulent wake signal lost any semblance of its original shape. However, there is a broad signal from a depth of -40 to a depth of -80-meters that extends diagonally downward and is centered at 100 meters on the y. This appears to be the bulk of the remaining wake signature; however, differentiating between the direct wake signature and the billowing turbulence becomes increasingly difficult as time progresses. This will become especially relevant in our discussion of the signal in the turbulent case in Section 3.3. By an hour after passage (Nt = 20.60), the remaining signal is indistinguishable from turbulence that rose from the lower half of the domain.

Figure 3.3, presents the evolution of $\overline{\varepsilon}$ in the same manner as in Figure 3.2. The morphology over time for $\overline{\varepsilon}$ follows similar behavior to that of $\overline{\chi}$. However, both the quiescent and the turbulent initial signals are 2–3 orders of magnitude higher than the initial $\overline{\chi}$ signals. Next, as the wake collapses in the quiescent case, starting at Nt = 10.31, the $\overline{\varepsilon}$ signals remain well defined whereas those in $\overline{\chi}$ become more diffuse. During the same time for the turbulent

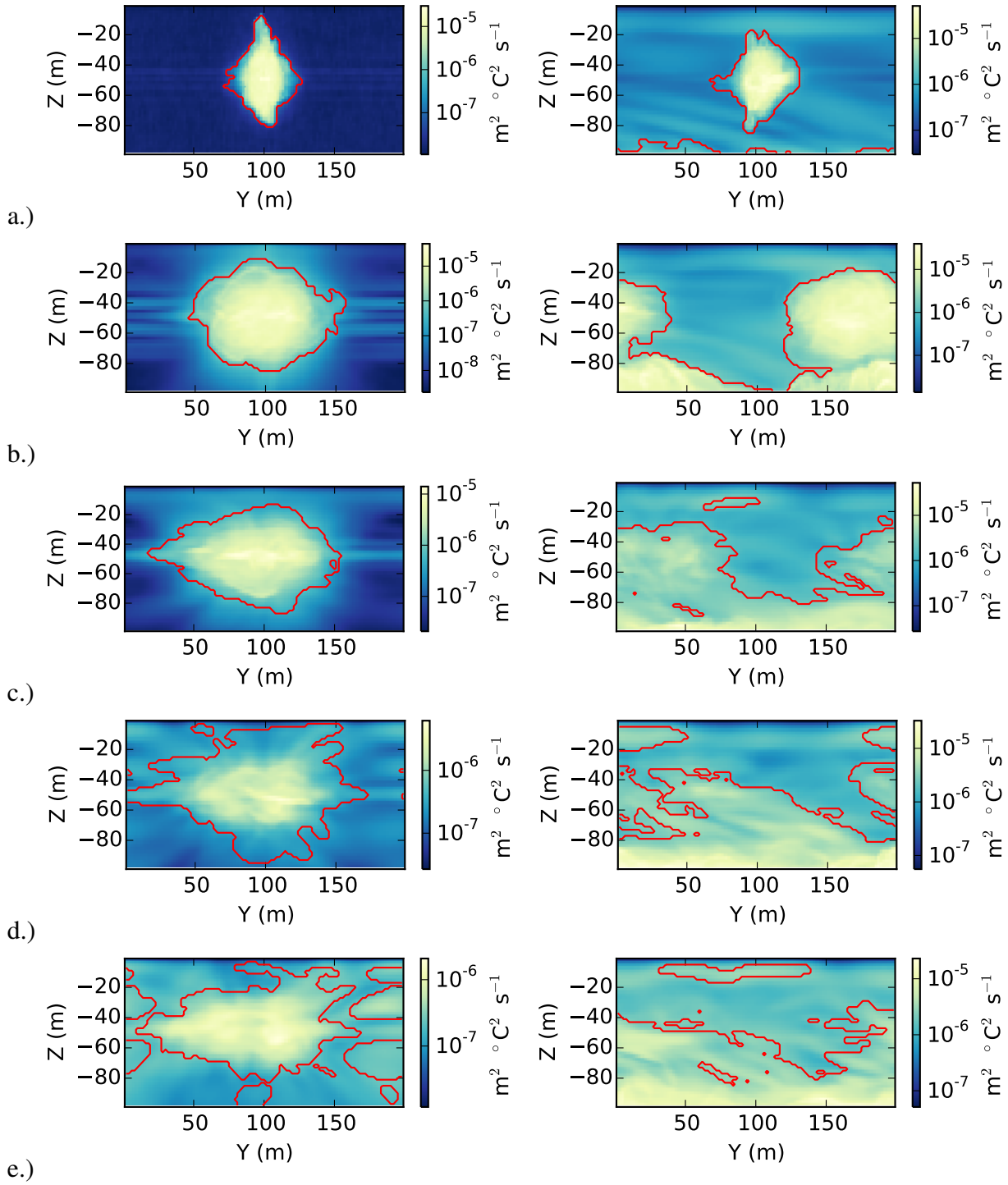

Figure 3.2. A time-lapse yz-plane view of $\overline{\chi}$ after SB passage. The red contour outlines the mask, m. Run 1 is down the left column and Run 2 is down the right column. a.) Nt=0. b.) Nt=5.14 c.) Nt=10.31 d.) Nt=15.46 e.) Nt=20.60

cases, we observe the wake signature decaying, but the entrained turbulence signal persists at the same high values.

3.4 Dissipation Rates

In Figure 3.4 we examine the results from runs 1 and 5, quiescent cases focusing on the effects of submerged body depth on the mean threshold values of χ and ε. We compare this to the noise floor, as defined in Section 3.2, for a turbulent case with $\mathrm{Ri}_{avg} = 10$. Once the wake signals, $\langle\chi\rangle_\mathrm{t}$ and $\langle\varepsilon\rangle_\mathrm{t}$, reach the noise floor, detection becomes infeasible. We typically see that $\langle\varepsilon\rangle_\mathrm{t}$ is at its highest immediately after the submerged body passes ($t = 0$). After an initial plateau, $\langle\varepsilon\rangle_\mathrm{t}$ decays as a power law in time, which is anticipated for generic turbulent decay. The value of $\langle\varepsilon\rangle_\mathrm{t}$ is an integral measure of the small-scale turbulence in the wake, and this turbulence also serves to transport temperature, the effects of which are apparent in the delayed peak of $\langle\chi\rangle_\mathrm{t}$, once the turbulence has had enough time to mix the temperature field and produce a discernible $\langle\chi\rangle_\mathrm{t}$ signal. As with the turbulent dissipation rate, the thermal dissipation rate is also expected to decay as a power law in time after this peak. However, $\langle\chi\rangle_\mathrm{t}$, lags behind $\langle\varepsilon\rangle_\mathrm{t}$ and reaches the noise floor 15 minutes later.

Variations in depth have a minimal effect on the strength of the $\langle\chi\rangle_\mathrm{t}$ and $\langle\varepsilon\rangle_t$ signals. The turbulent dissipation rate of the -50-meter case increases in the same fashion as in the case of the shallow transit, but it reaches a maximum sooner, at $Nt = 2$. After this peak passes, the turbulent dissipation rate of the -50-meter case decreases at approximately the same rate as the shallower case and approaches the noise floor an hour after passage ($Nt = 20.60$). Since both $\langle\chi\rangle_\mathrm{t}$ and $\langle\varepsilon\rangle_t$ decay at approximately the same rate, the $\langle\varepsilon\rangle_t$ signal decays to the noise floor sooner, becoming indiscernible in approximately 45 minutes ($Nt = 15.46$).

Figure 3.5 examines the corresponding turbulent cases with varying depths, runs 3 and 6. For these simulations, the noise level is calculated by performing another simulation of with the same initial conditions as the turbulent case but in the absence of the submerged body. In both the -25-meter-depth and the -50-meter-depth cases, $\langle\chi\rangle_\mathrm{t}$ has a similar initial evolution as in the quiescent case, but two key features standout. The first is a second local maximum embedded in the underlying signal. This increase in $\langle\chi\rangle_\mathrm{t}$ occurs between $Nt = 2$ and $Nt = 5$ and corresponds with turbulence billowing up from the lower domain as shown in Figure 3.3. After the maximum is reached, $\langle\chi\rangle_\mathrm{t}$ decreases at approximately the

same rate as in the quiescent case until $Nt = 8$. At this point, for both the -25-meter and the -50-meter-depth cases, $\langle\chi\rangle_t$, reaches a quasi-steady state of approximately $4 - 5 \times 10^{-5}$ m^2 °C^2 s^{-1} and remains an order of magnitude above the noise floor. Because the noise floor is calculated for the same initial conditions, it is not expected that the billowing effect stems purely from the evolution of the turbulent boundary layer; instead, we anticipate that this effect is due to an interaction between the wake and the adjacent layer.

As with the case for $\langle\chi\rangle_t$, the turbulent $\langle\varepsilon\rangle_t$ is very similar to the quiescent case but with atypical local maxima near $Nt = 3$. This feature slightly precedes its equivalent peak in $\langle\chi\rangle_t$ and is the start of the turbulent entrainment from the lower domain into the upper domain. Beyond this maximum, $\langle\varepsilon\rangle_t$ continues to decay as before until reaching a quasi-steady state with a value of approximately 2×10^{-6} m^2 s^{-3}. Greater variability is observed for the -25-meter case beyond $Nt = 10$. In both the -25-meter and the -50-meter cases, $\langle\varepsilon\rangle_t$ remains approximately a factor of four above the noise floor.

Figure 3.6 demonstrates the effects of varying the submerged body's velocity in runs 1, 7, and 9 for the quiescent case while keeping the depth at -50 meters. The general evolution of the wake signatures in both $\langle\chi\rangle_t$ and $\langle\varepsilon\rangle_t$, follow the same pattern as the quiescent, depth-dependent cases. However, the variations in velocity have a greater effect on the initial values of $\langle\chi\rangle_t$ and $\langle\varepsilon\rangle_t$ than were observed when varying the depth. These observations are expected: higher velocities should impart more momentum to the surrounding environment, generating a stronger initial signal in $\langle\varepsilon\rangle_t$. These values span over an order of magnitude for $\langle\varepsilon\rangle_t$ which should require more time to decay for larger velocities. Despite some variability in the highest velocity case, all three cases show comparable decay rates, and the signals reach the noise floor within 30–60 minutes after the submerged body has passed. The slowest case, $u_{\max} = 2.5\text{ms}^{-1}$ reaches the noise floor near $Nt = 10.31$, and the fastest case, $u_{\max} = 10\text{ms}^{-1}$ near $Nt = 20.60$.

As is the case in the depth–dependent scenarios, the $\langle\chi\rangle_t$ signal lags behind $\langle\varepsilon\rangle_t$. However, the initial values are not as large as in $\langle\varepsilon\rangle_t$, and vary by a factor of three from the case with $u_{\max} = 2.5\text{ms}^{-1}$ to the case with $u_{\max} = 10\text{ms}^{-1}$. These simulations display similar behavior as in the depth–dependent case. The $u_{\max} = 5\text{ms}^{-1}$ and $u_{\max} = 10\text{ms}^{-1}$ simulations have the same decay rates; however, the dissipation rates in the simulation with $u_{\max} = 2.5\text{ms}^{-1}$ decay at a faster rate, reaching the noise floor between $Nt = 10.31$ and $Nt = 15.46$.

In Figure 3.7, we examine the turbulent cases with varying velocity, runs 3, 8, and 10. We see peaks in both $\langle\chi\rangle_t$ and $\langle\varepsilon\rangle_t$, with the $\langle\chi\rangle_t$ peak delayed as is typical. The general behavior of $\langle\varepsilon\rangle_t$ and $\langle\chi\rangle_t$, are consistent with those of the depth-dependent turbulent simulations. The peak in $\langle\varepsilon\rangle_t$, associated with entrained turbulence, as discussed previously, shows a slight temporal-dependence on $u_{\max}$, with $u_{\max} = 10\text{ms}^{-1}$ achieving a comparable value with $u_{\max} = 5\text{ms}^{-1}$, but delayed until $Nt = 3.5$. However, the entrainment in the $u_{\max} = 2.5\text{ms}^{-1}$ case, is a broad and shallow signal occurring between $Nt = 1$ and $Nt = 2.5$. This is attributed to the weakness of the interaction between the wake signature with the adjacent boundary layer and the wake's inability to entrain large amounts of turbulence from the lower domain. However, we see that for $u_{\max} = 10\text{ms}^{-1}$, the maximum $\langle\chi\rangle_t$ value is higher compared with the two slower cases. This is due to the entrained $\langle\chi\rangle_t$ signal being added to the already elevated wake signature. This is largely consistent with the physical processes we've described to this point of the turbulence mixing the temperature field and generating a later peak in chi.

In Figure 3.8, we examine the effects of varying the mean Richardson number prior to the submerged body's transit while keeping the depth at -50 m and velocity at 5 m/s by analyzing runs 2–4. We observe negligible differences in $\langle\varepsilon\rangle_\text{t}$ between the low-Ri case(Ri = 5) and the high-Ri case (Ri = 20). Neither simulation displays the turbulent entrainment that was clear in the depth or velocity-dependent cases until $Nt = 8$. Afterwards, the low-Ri and high-Ri cases' behave more in line with what is expected from the previous turbulent cases. The low-Ri case reaches a quasi-steady state after entraining turbulence from the lower domain. The high-Ri case continues to decay before settling at a quasi-steady state which is weaker than the other two cases. The low-Ri and high-Ri simulations both have $\langle\chi\rangle_\text{t}$ signals that are very similar to the quiescent, depth-dependent scenario, with the exception that the turbulent low-Ri and high-Ri cases reach their maxima earlier than the quiescent case. Both the low-Ri and high-Ri cases behave comparably until $Nt = 8$, at which point, the low-Ri dissipation rate increases as an indication that turbulence is being entrained. The moderate-Ri simulation (Ri = 10) shows the most unique behavior, showing the strongest indication of turbulent entrainment. As shown in Table 3.2, the moderate-Ri case also corresponds to the highest Brunt-Väisälä frequency, N, which may lead to a stronger vertical gradient of N across the boundary layer separating the upper and lower regions of the domain. This could result in a more volatile interface and hence promote entrainment.

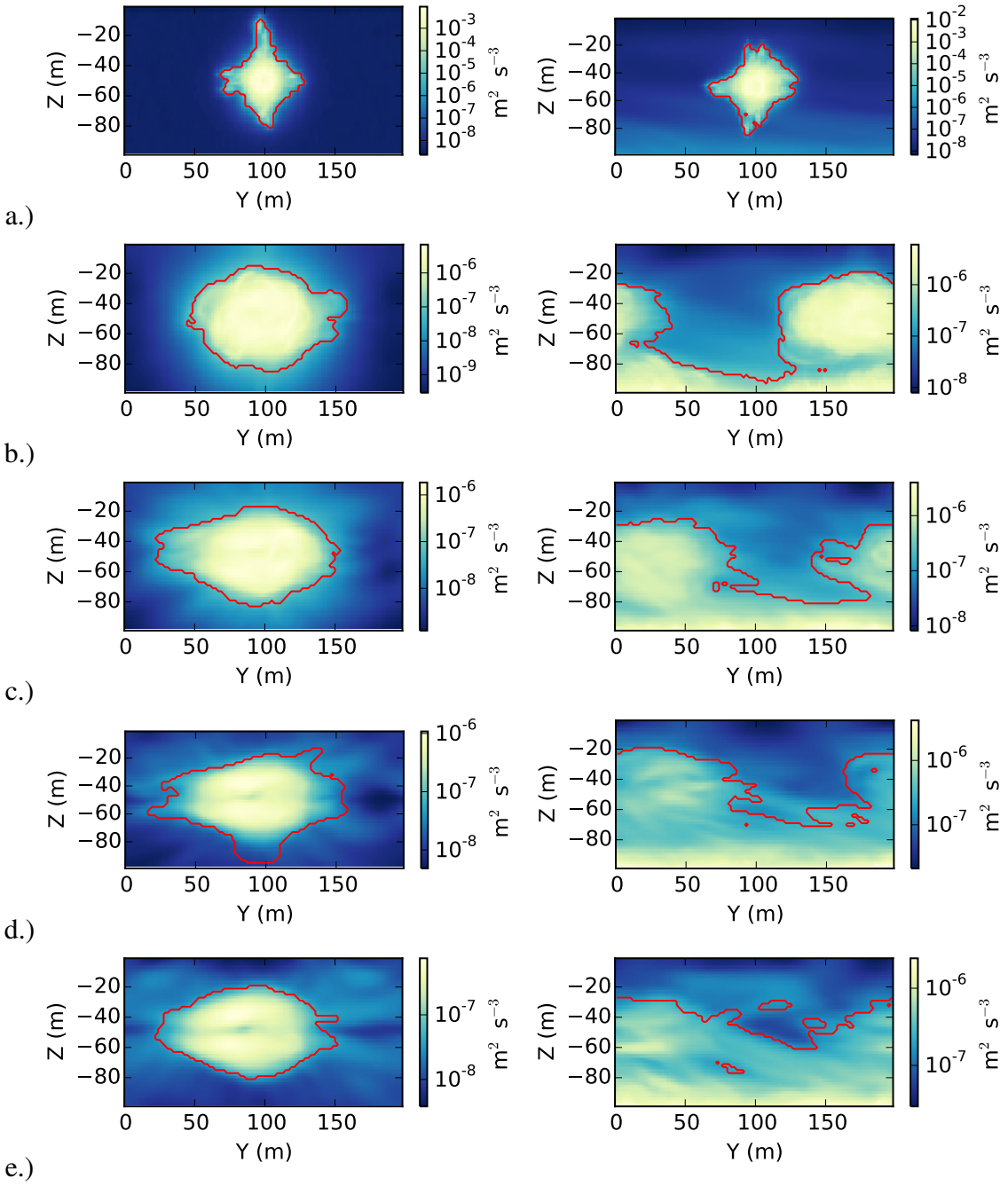

Figure 3.3. A time-lapse yz-plane view of $\overline{\varepsilon}$ after SB passage. The red contour outlines the mask, m. Run 1 is down the left column and Run 2 is down the right column. a.) Nt=0. b.) Nt=5.14 c.) Nt=10.31 d.) Nt=15.46 e.) Nt=20.60

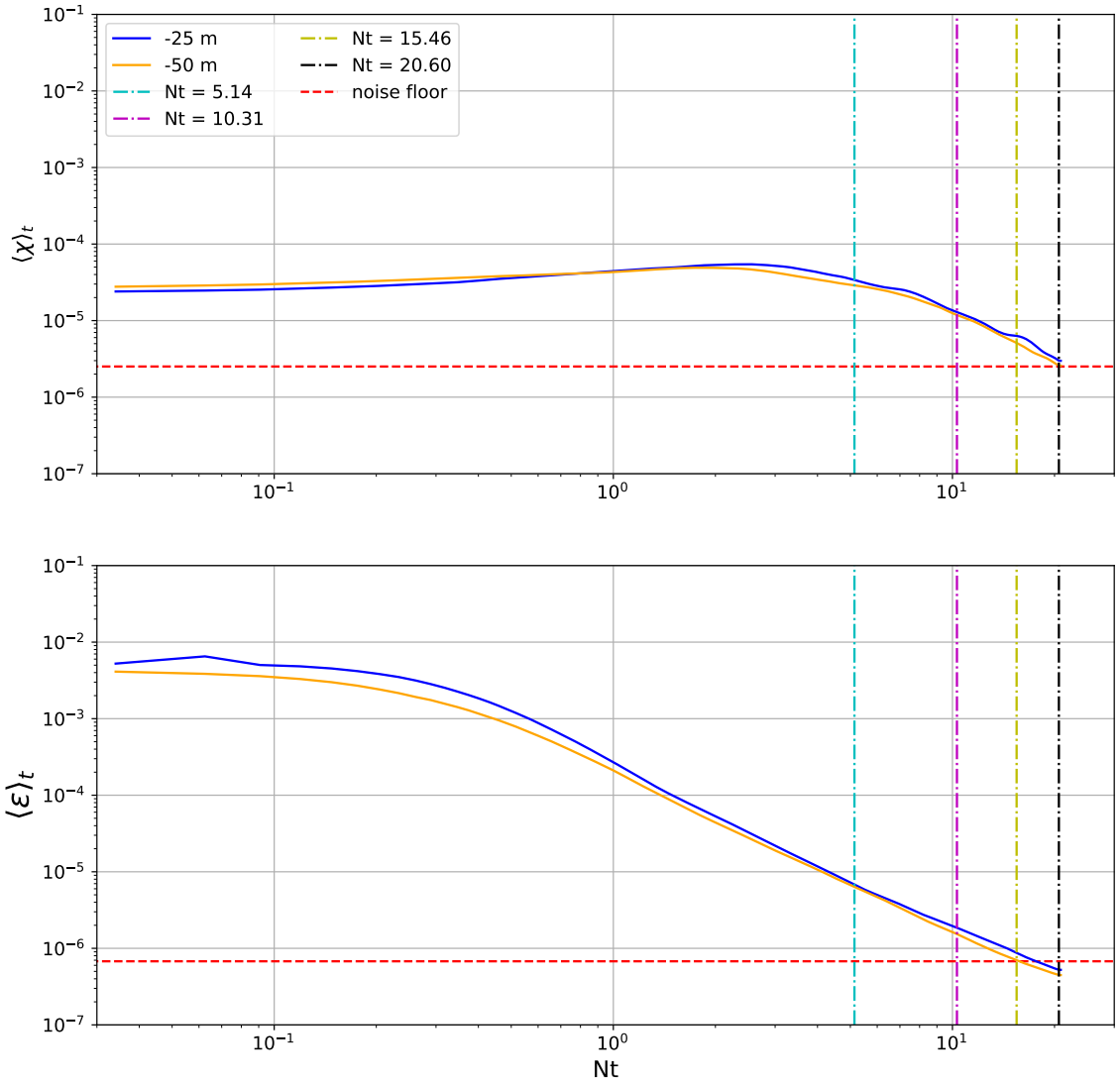

Figure 3.4. For the quiescent case $\langle\chi\rangle_t$ and $\langle\varepsilon\rangle_t$ are plotted on the ordinate axes, with Nt on the abscissa. The solid blue and orange lines depict the evolution of $\langle\chi\rangle_t$ and $\langle\varepsilon\rangle_t$ when the SB transited at a depth of -25 meters and -50 meters . The dashed red line is the noise floor calculated over 1 tidal cycle prior to the SB passage. The cyan, magenta, yellow, and black dash-dotted lines correspond to an Nt of 5.14, 10.31, 15.46 and 20.60, which correspond to the times of the snapshots presented in Figures 3.2 and 3.3

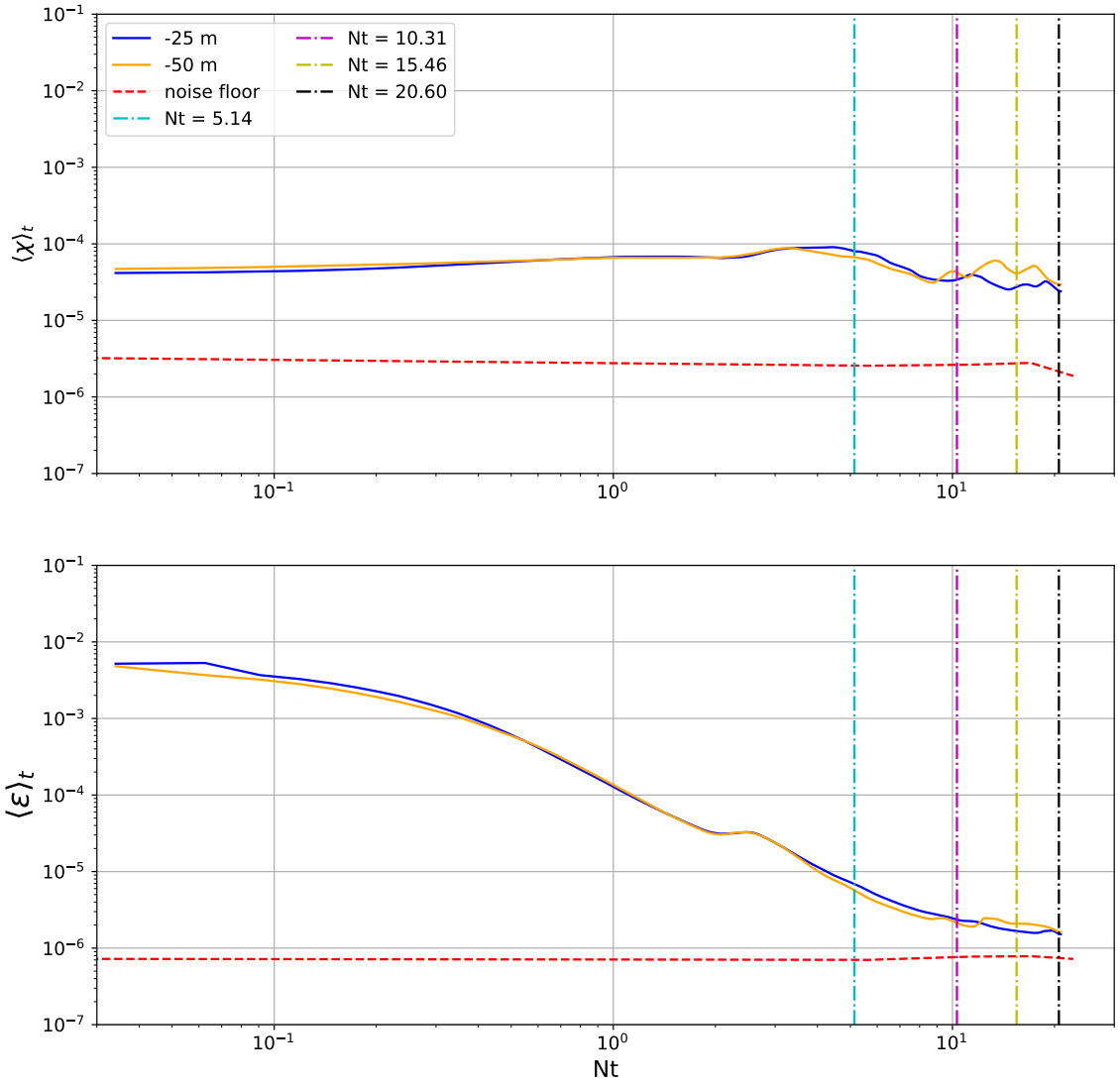

Figure 3.5. The quantities $\langle\chi\rangle_t$ and $\langle\varepsilon\rangle_t$ are plotted for the depth-dependent turbulent cases in the same manner as in Figure 3.4. The dashed red line instead shows the noise evolution during the same time period over which the wake evolves without the impact of the SB.

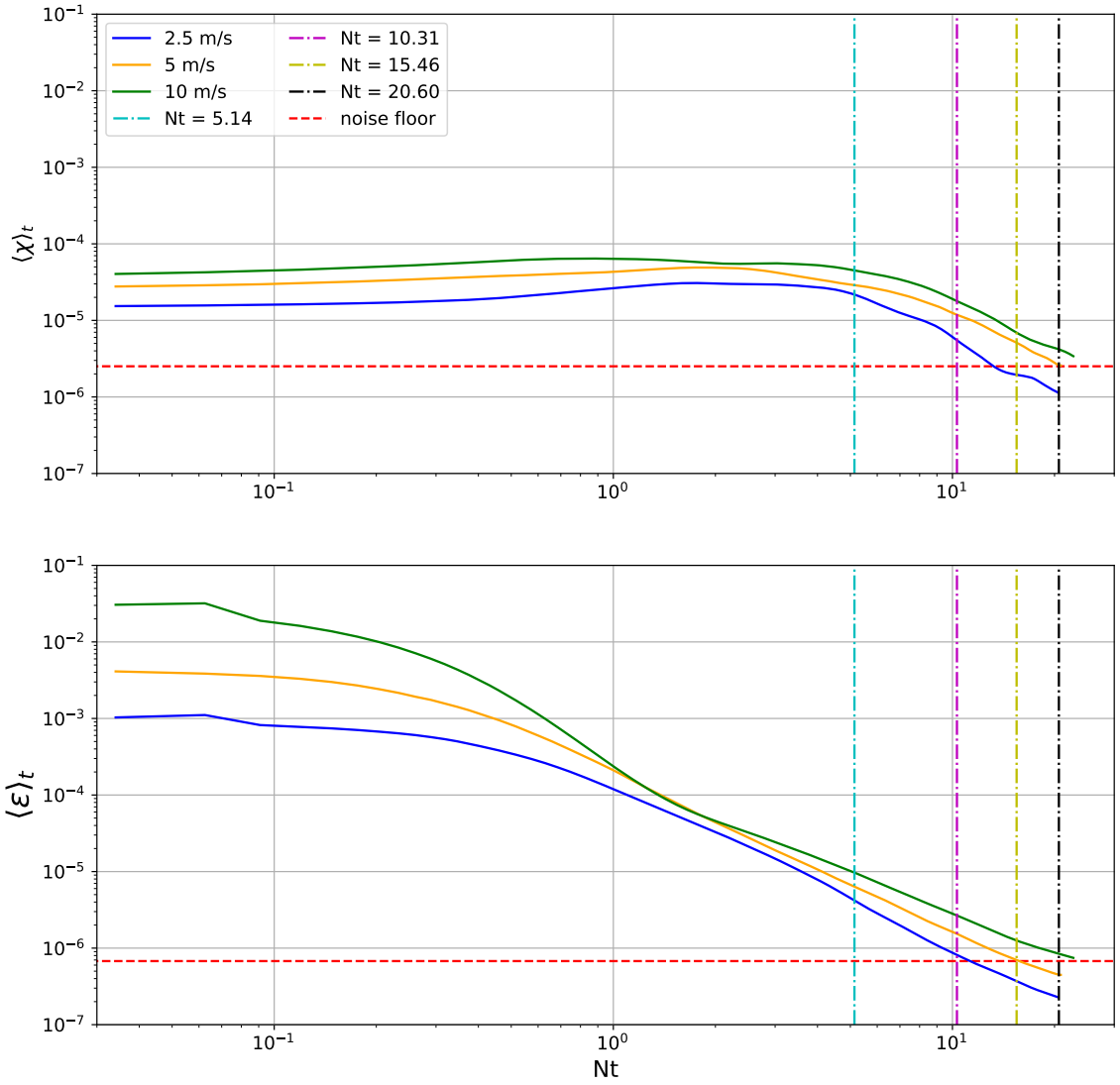

Figure 3.6. The quantities $\langle\chi\rangle_t$ and $\langle\varepsilon\rangle_t$ are plotted for the velocity-dependent quiescent cases in the manner as in Figure 3.4. The solid blue, orange, and green lines depict the evolution of $\langle\chi\rangle_t$ and $\langle\varepsilon\rangle_t$ when the SB transited at a velocity of 2.5 m/s, 5 m/s, and 10 m/s, respectively.

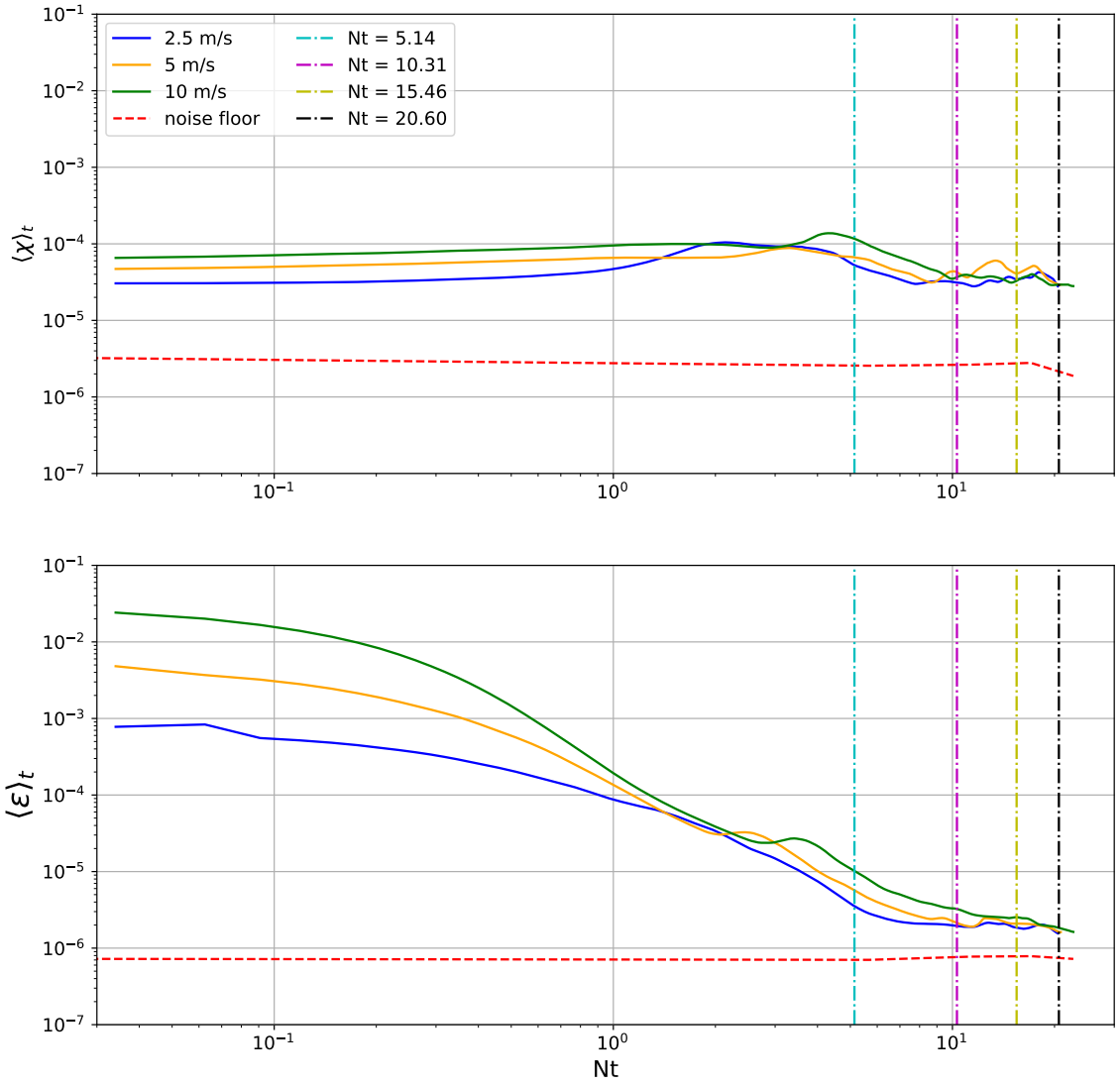

Figure 3.7. The quantities $\langle\chi\rangle_t$ and $\langle\varepsilon\rangle_t$ are plotted for the velocity-dependent turbulent cases in the same manner as in Figure 3.5. The solid blue, orange, and green lines depict the evolution of $\langle\chi\rangle_t$ and $\langle\varepsilon\rangle_t$ when the SB transited at a velocity of 2.5 m/s, 5 m/s, and 10 m/s, respectively.

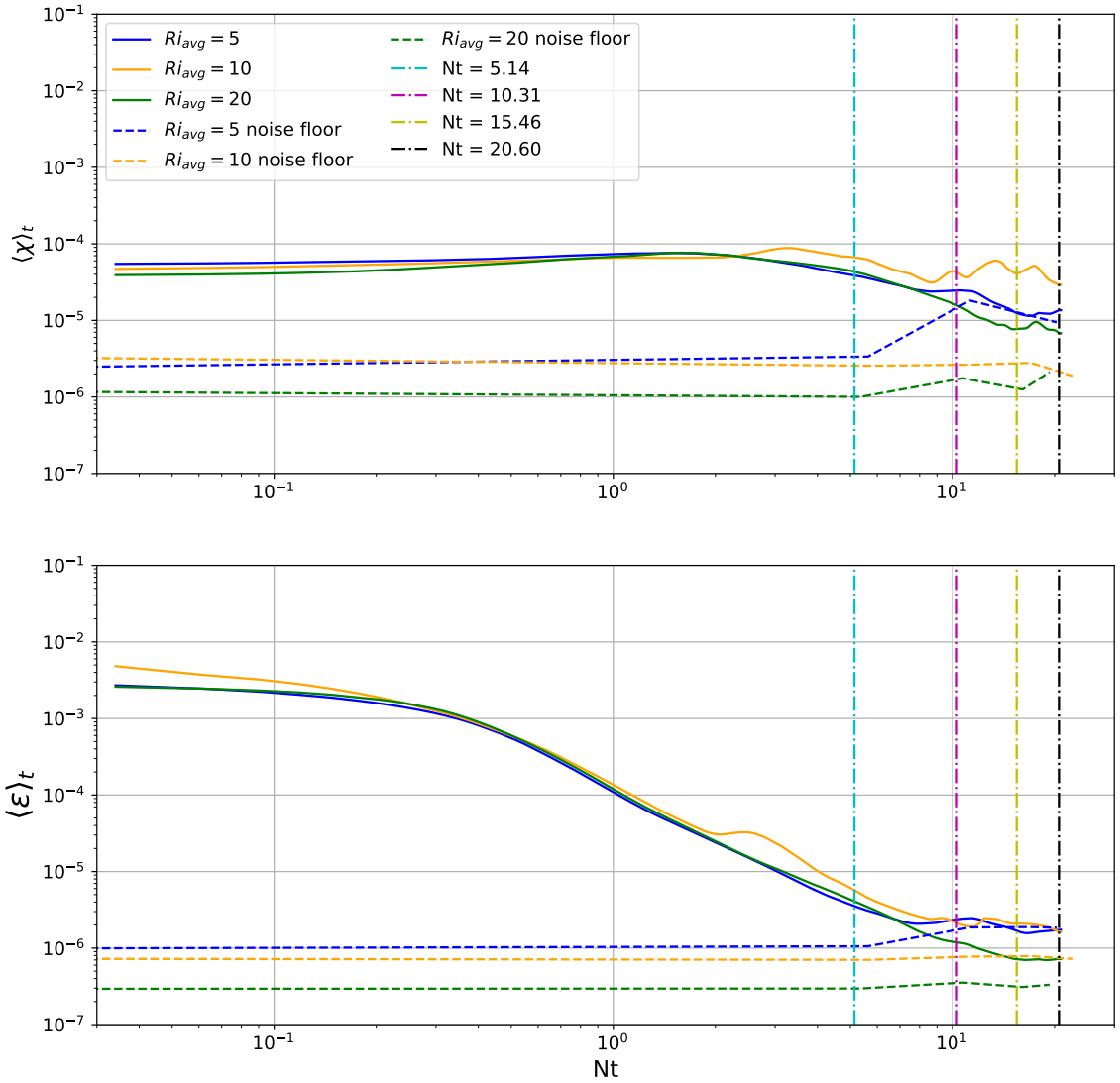

Figure 3.8. The quantities $\langle \chi \rangle_t$ and $\langle \varepsilon \rangle_t$ are plotted for the Richardson-number-dependent cases. The solid blue, orange, and green lines depict the evolution of $\langle \chi \rangle_t$ and $\langle \varepsilon \rangle_t$ for the case where Ri_{avg} is 5, 10, and 20, respectively

THIS PAGE INTENTIONALLY LEFT BLANK

CHAPTER 4:
Discussion

4.1 Conclusions

In this study, we examined the interactions between a stratified wake produced by a towed ellipsoid and an internal wave field. The submerged body's wake produced a signature in the dissipation rates, χ and ε, which have a dependence on depth, velocity and the mean Richardson number. From these, we were able to draw four main conclusions describing the interaction between the direct wake and the internal wave field, a noise floor for $\langle\chi\rangle_t$ and $\langle\varepsilon\rangle_t$, a signal to noise ratio, and the interactions between the wake and the boundary layer.

First, in both $\langle\chi\rangle_t$ and $\langle\varepsilon\rangle_t$, there were no observable interactions between the direct wake from the submerged body and the background internal wave field. The differences observed when comparing the quiescent cases to the turbulent cases can be attributed to the turbulence that is entrained from the lower portion of the domain. Second, distinct baselines for $\langle\chi\rangle_t$ and $\langle\varepsilon\rangle_t$ were derived for three distinct mean Richardson numbers as described in Table 3.2. We interpret the baselines as a background noise floor. Insight into a signal to noise ratio can be obtained when the quiescent wake signatures are compared to this floor. Third, a comparison of the quiescent wake signatures showed that regardless of depth or velocity variation, the dissipation rates, $\langle\chi\rangle_t$ and $\langle\varepsilon\rangle_t$, fell below the typical oceanic noise within 45–60 minutes, which would render the wake signature indiscernible by direct measurements of the wake using χ and ε.

Finally, the wake from a submerged body can influence a nearby boundary between a more turbulent layer and more stable layer. This can lead to turbulence not associated with the wake of the submerged body to be entrained into the region of interest, such as in the stable region below a surface mixed layer. The resultant $\langle\chi\rangle_t$ or $\langle\varepsilon\rangle_t$ signatures could persist longer and provide an indirect measurement of the submerged body's wake. We found that for both depths, there were negligible differences in the maximum values of $\langle\chi\rangle_t$ and $\langle\varepsilon\rangle_t$, or in when they occurred. In the velocity-dependent cases, we observed that the $\langle\chi\rangle_t$ and $\langle\varepsilon\rangle_t$ maximum values associated with this entrainment lagged behind the simulations

with slower submerged bodies. There was slight variability in the maximum values of $\langle\chi\rangle_t$ and $\langle\varepsilon\rangle_t$ with the faster velocities generating more turbulence. Lastly, for the Richardson-number-dependent cases we observed a significant difference in our Ri = 10 case compared to cases with higher or lower Richardson numbers. This can be attributed to the fact that the moderate-Ri case had the highest Brunt-Väisälä frequency. This sets up a larger difference in N between the upper and lower domains, resulting in a more volatile boundary layer.

4.2 Operational Relevance

For all the technological advancements that can be made to reflect and dampen acoustic energy, when a submarine transits through the ocean, it will leave behind either a direct or indirect hydrodynamic signature which may last for several hours. One possible way to calculate these signatures is with the dissipation rates χ and ε. To calculate these quantities in the real ocean, the three-dimensional temperature and velocity gradients would ordinarily need to be determined. Due to the nature of oceanographic instruments, however, obtaining these three-dimensional gradients from in situ data is often impractical. A common approach used in oceanographic microstructure measurements would be deploying instrumentation that only measures gradients in one dimension, which can be used to approximate the three-dimensional gradients via assumptions of isotropy and incompressibility. Sonar buoys and unmanned underwater vehicles are often equipped with a conductivity, temperature, and depth (CTD) sensor or an acoustic Doppler current profiler (ADCP), and could be deployed to collect this vital data. However, χ and ε, are difficult to observe remotely. Therefore, a remote sensing application would require a different parameter set to analyze potential surface features.

4.3 Future Research

This study provides several avenues for additional research. One such topic is a similar analysis of surface features produced by the submerged body's transit. In particular, temperature perturbations and surface heights can be observed with airborne or satellite assets. If the fine structures of these parameters can be observed against the background of sea surface waves, then an aerial view could provide a larger region that could be searched quicker. Another study of immediate interest could contain a series of numerical experiments of a

submerged body below a mixed layer in order to further investigate the effects of a transiting body on the entrainment of the turbulence from nearby regions. This would provide insight into the structure of the wake signature after passing through a boundary and reaching the sea surface.

THIS PAGE INTENTIONALLY LEFT BLANK

List of References

[1] H.-P. Pao and T. W. Kao, "Vortex structure in the wake of a sphere," *American Institute of Physics*, vol. 187, no. 20, p. 6, 1977.

[2] J.-T. Linl and Y.-H. Pao, "Wakes in Stratified Fluids," *Annual Review of Fluid Mechanics*, p. 22, 1979.

[3] G. R. Spedding, "The evolution of initially turbulent bluff-body wakes at high internal Froude number," *Journal of Fluid Mechanics*, vol. 337, pp. 283–301, Apr. 1997.

[4] T. Radko and D. Lorfeld, "Effects of weak planetary rotation on the stability and dynamics of internal stratified jets," *Physics of Fluids*, vol. 30, no. 9, p. 096602, Sep. 2018.

[5] S. I. Voropayev, H. J. S. Fernando, S. A. Smirnov, and R. Morrison, "On surface signatures generated by submerged momentum sources," *Physics of Fluids*, vol. 19, no. 7, p. 076603, July 2007.

[6] Z. E. Moody, C. J. Merriam, T. Radko, and J. Joseph, "On the structure and dynamics of stratified wakes generated by submerged propagating objects," *Journal of Operational Oceanography*, vol. 10, no. 2, pp. 191–204, Apr. 2017.

[7] T. Radko and D. Lewis, "The age of a wake," *Physics of Fluids*, vol. 31, no. 7, p. 076601, July 2019.

[8] J. Marshall, A. Adcroft, C. Hill, L. Perelman, and C. Heisey, "A finite-volume, incompressible Navier Stokes model for studies of the ocean on parallel computers," *Journal of Geophysical Research: Oceans*, vol. 102, no. C3, pp. 5753–5766, Mar. 1997.

[9] J. A. Goff and T. H. Jordan, "Stochastic modeling of seafloor morphology: Inversion of sea beam data for second-order statistics," *Journal of Geophysical Research: Solid Earth*, vol. 93, no. B11, pp. 13 589–13 608, Nov. 1988.

THIS PAGE INTENTIONALLY LEFT BLANK

Initial Distribution List

1. Defense Technical Information Center
   Ft. Belvoir, Virginia

2. Dudley Knox Library
   Naval Postgraduate School
   Monterey, California